Nonmuscle myosin IIA and IIB differentially modulate migration and alter gene expression in primary mouse tumorigenic cells

Debdatta Halder[a], Shekhar Saha[a,b], Raman K. Singh[a,c], Indranil Ghosh[a], Ditipriya Mallick[a], Sumit K. Dey[a,d], Arijit Ghosh[a], Benu Brata Das[a], Somiranjan Ghosh[e], and Siddhartha S. Jana[a,*]

[a]School of Biological Sciences, Indian Association for the Cultivation of Science, Jadavpur, Kolkata 700032, India; [b]Department of Biochemistry and Molecular Genetics, University of Virginia, Charlottesville, VA 22908; [c]Department of Molecular Genetics, Weizmann Institute of Science, Rehovot 7610010, Israel; [d]Department of Biological and Environmental Engineering, Cornell University, Ithaca, NY 14853; [e]Department of Biology, Howard University, Washington, DC 20059

ABSTRACT **Though many cancers are known to show up-regulation of nonmuscle myosin (NM) IIA and IIB, the mechanism by which NMIIs aid in cancer development remains unexplored. Here we demonstrate that tumor-generating, fibroblast-like cells isolated from 3-methylcholanthrene (3MC)-induced murine tumor exhibit distinct phospho-dependent localization of NMIIA and NMIIB at the perinuclear area and tip of the filopodia and affect cell migration differentially. While NMIIA-KD affects protrusion dynamics and increases cell directionality, NMIIB-KD lowers migration speed and increases filopodial branching. Strategically located NMIIs at the perinuclear area colocalize with the linker of nucleoskeleton and cytoskeleton (LINC) protein Nesprin2 and maintain the integrity of the nuclear-actin cap. Interestingly, knockdown of NMIIs results in altered expression of genes involved in epithelial-to-mesenchymal transition, angiogenesis, and cellular senescence. NMIIB-KD cells display down-regulation of Gsc and Serpinb2, which is strikingly similar to Nesprin2-KD cells as assessed by quantitative PCR analysis. Further gene network analysis predicts that NMIIA and NMIIB may act on similar pathways but through different regulators. Concomitantly, knockdown of NMIIA or NMIIB lowers the growth rate and tumor volume of 3MC-induced tumor in vivo. Altogether, these results open a new window to further investigate the effect of LINC-associated perinuclear actomyosin complex on mechanoresponsive gene expression in the growing tumor.**

Monitoring Editor
Dennis Discher
University of Pennsylvania

Received: Dec 13, 2018
Revised: Apr 4, 2019
Accepted: Apr 10, 2019

INTRODUCTION

NMIIs are hexameric actin-binding motor proteins, composed of one pair of heavy chains (NMHC), a pair of essential light chains (ELC), and a pair of regulatory light chains (RLC; Coluccio, 2008). The three different paralogues, NMIIA, NMIIB, and NMIIC, are named on the basis of their heavy chains, encoded by Myh9, Myh10, and Myh14 genes, respectively, in mammals. NMII can exist as motor-active monomers and oligomers in a cell (Vicente-Manzanares *et al.*, 2009). Contractile force in a cell is mainly generated when

This article was published online ahead of print in MBoC in Press (http://www.molbiolcell.org/cgi/doi/10.1091/mbc.E18-12-0790) on April 17, 2019.

No potential conflicts of interest were disclosed by the authors.

D.H., S.S., and S.S.J. designed the research. D.H., S.S., R.K.S., I.G., D.M., S.K.D., A.G., and S.G. performed research. D.H., R.K.S., and S.G. analyzed the data. A.G. and B.B.D. contributed analytic tools. D.H. and S.S.J. wrote the manuscript. All other authors reviewed the manuscript.

*Address correspondence to: Siddhartha Sankar Jana (bcssj@iacs.res.in).

Abbreviations used: Angpt1, angiopoetin 1; CK II, casein kinase II; CP, canonical pathway; CTGF, connective tissue growth factor; Gsc, goosecoid; H&E, hematoxylin and eosin red; IPA, ingenuity pathway analysis; KD, knockdown; LINC, linker of nucleoskeleton and cytoskeleton; LPA, lysophosphatidic acid; 3MC, 3-methylcholanthrene; MLCK, myosin light chain kinase; NMHC II, nonmuscle myosin heavy chain II; NMII, nonmuscle myosin II; PCNA, proliferation cell nuclear antigen; RLC, regulatory light chain; ROCK, Rho-associated coiled coil containing kinase; RT-PCR, reverse transcription-PCR; siRNA, small interfering RNA; SMA, smooth muscle actin; TAN, transmembrane actin–associated nuclear lines; Tbx2, T-box transcription factor; TRPM7, transient receptor potential melastatin 7; YAP/TAZ, yes-associated protein/tafazzin.

monomers are incorporated into bipolar filaments, and it participates in cell–substrate adhesion, leading edge protrusion, cell body translocation, and cell polarity during cellular migration. NMII is also needed for cytokinesis, invasion, metastatic dissemination, etc. (Coluccio, 2008; Conti and Adelstein, 2008; Vicente-Manzanares *et al.*, 2009; Aguilar-Cuenca *et al.*, 2014; Shutova and Svitkina, 2018). The importance of the monomeric form of NMII has been established in endocytosis, exocytosis, and vesicular transport (Shutova and Svitkina, 2018). NMII paralogues may participate in similar or distinctly different cellular functions (Dey *et al.*, 2017; Shutova and Svitkina, 2018). NMII are regulated by many kinases such as MLCK (myosin light chain kinase), Rho-ROCK (Rho-associated kinase), protein kinase C, CK, and TRPM7, which are involved in phosphorylation of either RLC or HC, to maintain the dynamics among motor-inactive and active monomers, and oligomers in the cells (Vicente-Manzanares *et al.*, 2009). Expression of such NMII regulators as well as NMII paralogues has been reported to be altered in several cancers (Newell-Litwa *et al.*, 2015).

Several studies suggested that NMIIA promotes the progression of various types of cancers or acts as a tumor suppressor (Pecci *et al.*, 2018), suggesting context-dependent function of NMIIA in cancerous cells. Many tumors also show a high expression of NMIIB, which associates with poor prognosis and metastasis (Newell-Litwa *et al.*, 2015). NMIIC1, a spliced isoform of NMIIC, on the other hand, has been reported to play a critical role in ring formation during cytokinesis of breast cancer cells, disruption of which results in aberrant cell division and chromosome instability (Takaoka *et al.*, 2014). Long noncoding RNA (lncRNA) corresponding to NMIIC has also been found to be highly up-regulated in lung adenocarcinoma in human patients, indicating the possible involvement of NMII in cancer progression (Zhang *et al.*, 2017). 3-Methylcholanthrene (3MC)-induced tumor in mice is a well-known model for studying cancer development (Thakker *et al.*, 1978; Qin *et al.*, 2002). Recent findings reveal that transformation of normal skeletal muscle to tumor tissue is associated with an alteration of fibroblast-like cells to atypical cells showing enlarged vesicular nuclei, prominent nucleoli, and heterogeneous morphology. These cells, when isolated from the tumor, grow as atypical fibroblast-like cells in transient culture and are capable of forming tumors in immunodeficient mice (Koebel *et al.*, 2007; Saha *et al.*, 2011). Also, 3MC-induced tumor development is associated with increased expression of NMIIA and NMIIB in vivo (Saha *et al.*, 2011). However, the mechanisms by which NMIIs in these transformed cells contribute to cancer progression remain poorly understood.

Here, we show for the first time that the tumorigenic cells isolated from 3MC-induced tumor tissue express both NMIIA and NMIIB. These cells also express myofibroblast marker α-SMA, Vimentin, and cancer stem cell marker, CD34. Both NMIIA and NMIIB localize at the tip of protrusion and are found to be colocalized with the LINC protein Nesprin2 at the perinuclear actin network. Small interfering RNA (siRNA)-mediated knockdown of either of the NM II paralogues differentially inhibits cellular migration in the isolated tumorigenic cells and reduces tumor growth in vivo. Also, NMIIs modulate the expression of genes associated with cancer progression, suggesting the possibility of involvement of NMIIA and NMIIB in the mechanotransduction pathways, during tumor progression.

RESULTS

Proliferative cells in 3MC-induced tumor expressing NMIIA and NMIIB are tumorigenic

Intramuscular injection of 3MC in the hind limb of mice generates visible tumors within 89 d, and tumor formation is associated with the transformation of fibroblast-like cells to atypical cells and their proliferation (Koebel *et al.*, 2007; Saha *et al.*, 2011). To follow the transformation and proliferation of the cells during tumor progression, we performed hematoxylin and eosin red (H&E) and proliferation cell nuclear antigen (PCNA) staining, respectively, of tissue sections focusing at the site of injection at every 7- to 15-d interval post–3MC regime as shown in Figure 1A. We noticed the loss of organized structure of the muscle, and signs of proliferation at the site of 3MC injection at 59 d compared with olive oil–treated tissue, which maintained the organized structure at all the time points. Furthermore, we found early signs of proliferation at 44 d near the lipid droplets (site of injection) but we could not detect visible signs of tissue transformation before 59 d. At 89–110 d when the tumor was of visible size, a majority of the cells were transformed and proliferative, whereas no such proliferation or structural loss was detectable even at 7 d (Figure 1, B and C), suggesting that 3MC may cause transformation and proliferation not before 44–59 d at the site of injection. The expression of cytosolic motor proteins NMIIA and NMIIB was shown to be increased in the tumor but not in the normal tissue associated with tumors (Koebel *et al.*, 2007; Saha *et al.*, 2011). We were interested to know whether the cells in the transformed area at 59 d expressed NMIIA and NMIIB. Figure 1D shows that the transformed cells (delineated by arrowheads) expressed NMIIA at 59 d but not NMIIB, which was detectable only at a later time point, 89 d (Supplemental Figure S1). 3MC tumors are known to originate from the site of injection and often form fibrosarcomas (Qin *et al.*, 2002), so we were interested to look for the markers of myofibroblast in the transformed areas. Additionally, at both 59 and 89 d, these cells showed the expression of α-SMA, Vimentin, and CD34, indicating that they are fibroblast-like (myofibroblast) and might have stemness properties (Figure 1D and Supplemental Figure S1). To evaluate the potential function of NMIIA and NMIIB in these cells, we isolated them at 89–95 d and cultured them in vitro. Fluorescence-activated cell sorting (FACS) analysis shows that more than 90% of the isolated cells express α-SMA, Vimentin, and CD34, along with NMIIA and NMIIB (Figure 1E). Hence, they are likely to be $CD34^+$ fibroblasts. This is supported by immunofluorescence and immunoblotting of these cells and cell lysates with the respective antibodies (Supplemental Figure S2, A and B). The isolated cells when subcutaneously transplanted in athymic nude mice generated tumors within 10–15 d postinjection (Supplemental Figure S2, C and D). Altogether, these data suggest that both proliferation and transformation in the tissue are detectable as early as 44–59 d. Proliferative cells expressing NMIIA at early stages and both NMIIs at later stages are myofibroblasts in nature, and the isolated myofibroblasts are tumorigenic.

MLCK regulates the localization of NMIIA and NMIIB at the protrusive ends and perinuclear region in the primary tumorigenic cells

We wished to check the localization of NMIIs in the tumorigenic cells. Both NMIIA and NMIIB are typically localized at the protrusive ends and perinuclear site along with their presence in stress fibers (Figure 2, A and B, top panels, and Supplemental Figure S3A). NMIIs are phosphorylated both at the protrusive ends and perinuclear sites as detected by staining with a phospho-specific antibody against RLC (Supplemental Figure S3, B and C), suggesting that NMIIs are active in these locations. RLC can be phosphorylated mainly by two orthogonal kinases: MLCK and ROCK (Kassianidou *et al.*, 2017). Next, we asked which kinase contributes to the phosphorylated NMIIs at the tip of the protrusion and perinuclear region. We treated the cells with ML-7, an inhibitor of MLCK, or Y27632, an inhibitor of ROCK kinase. Treatment of ML-7 but not Y27632 in

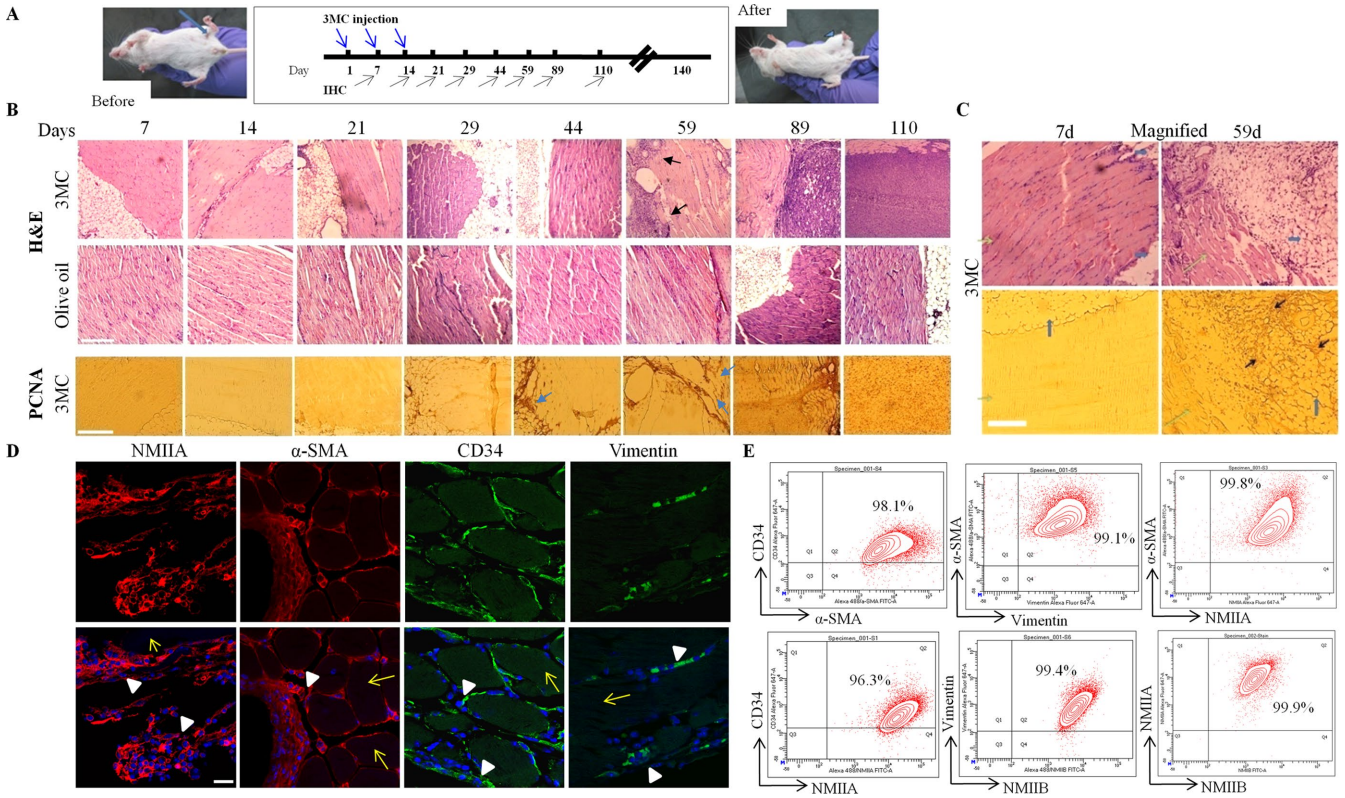

FIGURE 1: Cells at the site of injection start proliferating at 44–59 d and express NMIIA. (A) Schedule of 3MC injection and immunohistochemistry experiments. Representative image of a tumor formation at the site of 3MC injection shown in the left and right sides of the schedule. (B) Top and middle panels, H&E staining of 3MC- and olive oil–treated mouse tissue sections at indicated time points (white areas depict lipid droplets), respectively. Bottom panel, DAB staining for PCNA of analogous sections of 3MC-treated tissue sections at the same time points (blue arrows depict areas of proliferation; black arrows depict areas of transformation). (C) H&E (top panel) and PCNA/DAB (bottom panel) showing a comparison between the nontransformed section at 7 d (left panel) and partially transformed, proliferative cells at 59 d (right panel). Blue arrows indicate lipid droplets that mark the site of injection, black arrows indicate the PCNA positive/proliferative region, and light green arrows indicate the orderly structure of tissues. (D) Confocal immunofluorescence microscopy of analogous section of 59 d H&E of 3MC tissue sections probed with antibodies against NMIIA, Vimentin, α-SMA, or CD34. Yellow arrows indicate nontransformed regions, while transformed areas are delineated by arrowheads. (E) FACS contour plots of primary tumorigenic cells isolated at 89 d from 3MC-induced tumor in mice, fixed and stained with CD34, α-SMA, Vimentin, NMIIA, and NMIIB. Scale bars: 100 μm (B) and 20 μm (C, D).

primary tumorigenic cells reduced the amount of both NMIIA and NMIIB at the filopodial ends, suggesting that MLCK-dependent phosphorylation regulates NMII localization at this area (Figure 2, A, middle and bottom panels, and C). Interestingly, perinuclear NMIIA and NMIIB localization too was disrupted by ML-7 treatment (Figure 2, B, middle and bottom panels, and D). On the contrary, after Y27632 treatment, NMIIs were enriched around the nucleus and were confined to the SFs at the cell edge only. The intensity profile on the right-hand side shows that NMIIs displayed high fluorescence intensities around the nucleus in cells treated with Y27632, but not with ML-7, which showed equally distributed NMII fluorescence throughout the cell and loss of the distinct perinuclear intensity, suggesting that MLCK modulates perinuclear localization of NMIIs. The enrichment of NMIIs in the perinuclear area after ROCK inhibition may be due to enhanced activity of MLCK (Beach *et al.*, 2017). However, total amounts of NMIIA and NMIIB remain unchanged in the presence or absence of ML-7 or Y27632 (Supplemental Figure S3D). These data indicate that MLCK-dependent RLC phosphorylation of NMIIs is most likely needed for the localization of NMIIA and NMIIB at the filopodia tips and perinuclear region, whereas cytosolic NMII is regulated by ROCK.

NMIIA and NMIIB can assemble into apical actin network

We further assessed the relevance of the distinct localization of NMIIA and NMIIB around the nucleus by questioning what made them reside at the perinuclear position. The linker of nucleoskeleton and cytoskeleton (LINC) complex is composed of Nesprin proteins of the ONM (outer nuclear membrane) whose C-terminal KASH (Klarsicht, ANC-1, Syne homology) domain interacts with SUN (Sad1 Unc-84) domain–containing proteins of INM (inner nuclear membrane). Nesprin1 and 2 are known to interact with cytoskeletal actin through its calponin homology (CH) domains (Crisp *et al.*, 2006; Rajgor and Shanahan, 2013; Kirby and Lammerding, 2018). We were interested in checking whether actin-binding motor proteins NMIIA and NMIIB were able to interact with the LINC-actin filament complex. First, we checked the expression profile of actin-associated Nesprins in the primary tumor cells using the reverse transcription-PCR (RT-PCR) approach with primers designed against specific regions of Nesprin1 and 2 (Luxton *et al.*, 2010). Supplemental Figure S4A shows the presence of Nesprin2G (giant) but not Nesprin1G and other isoforms of Nesprin-1 and -2 in these cells. As the giant isoforms of Nesprin-1 and -2 are involved in the perinuclear LINC complex (Zhang *et al.*, 2001; Zhen *et al.*, 2002), and we could not

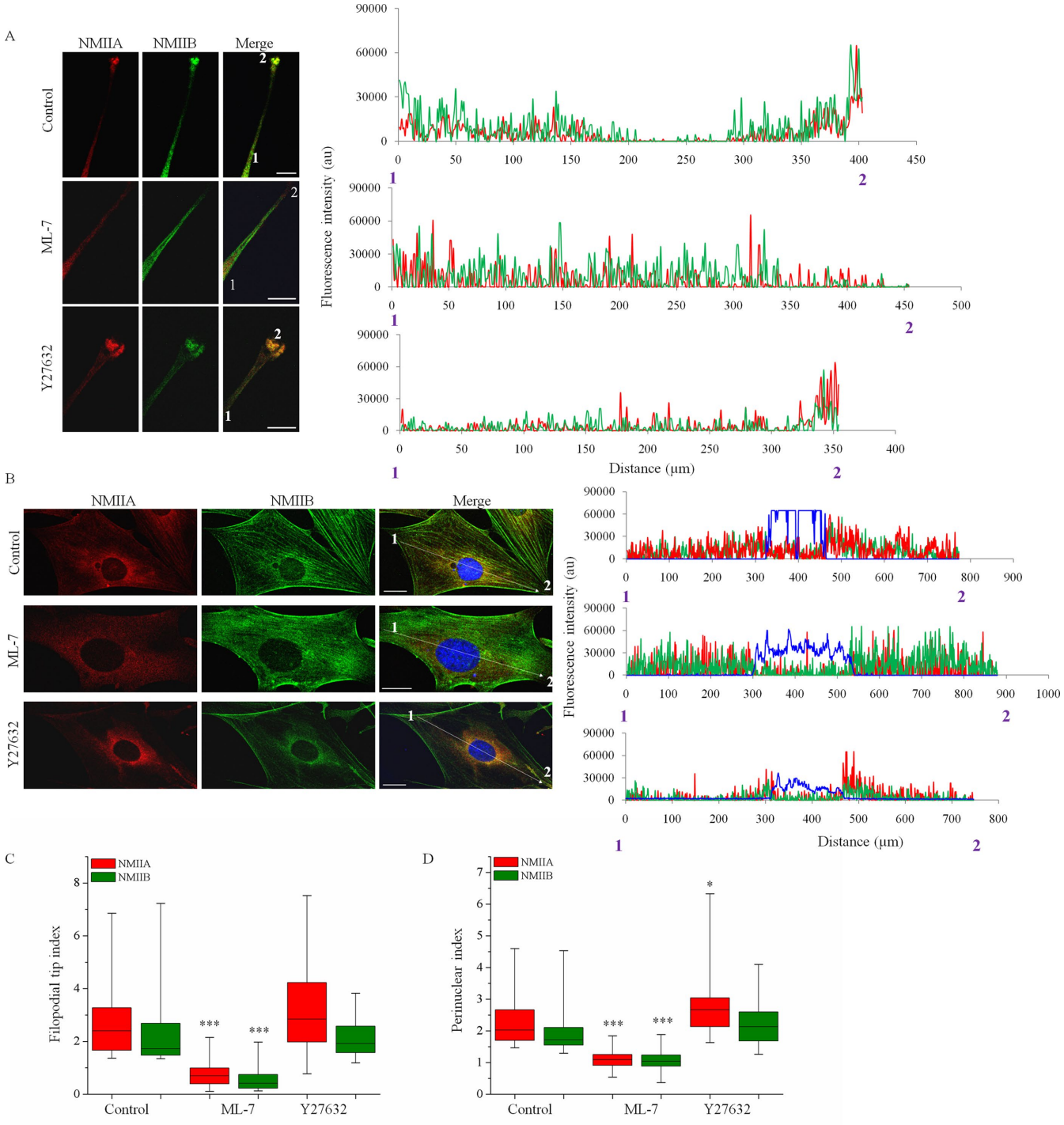

FIGURE 2: Localization of NMIIA and NMIIB at the filopodia tips and perinuclear area depends on MLCK. Confocal immunofluorescence microscopy of the primary tumorigenic cells probed with anti-NMIIA (red) and NMIIB (green) antibodies as shown at the (A) protrusions and (B) perinuclear area in the presence or absence of inhibitors for MLCK (ML-7) or Rho/ROCK kinase (Y27632). DAPI was used to stain the nucleus. Intensity graphs from position 1–2 are shown alongside the corresponding merge images. Box plot showing changes in (C) filopodial tip index (filopodial tip index = F.I. at tip/F.I. of whole filopodia) and (D) perinuclear index (perinuclear index = F.I. around the nucleus/F.I. of the whole cell) after ML-7 or Y27632 treatment in primary tumorigenic cells ($n > 30$ from three independent experiments). Scale bars: 10 μm (A) and 25 μm (B). ***, $P < 0.001$; control vs. ML-7 (NMIIA and NMIIB); *, $P < 0.05$; control vs. Y27632 (NMIIA, perinuclear area); F.I. was normalized against the area of ROI.

detect N1G, we proceeded with Nesprin-2 in the consequent experiments. We immunoprecipitated NMIIA or NMIIB using the specific antibody, and the immunoprecipitate was probed with Nesprin-2. Figure 3A shows multiple bands of Nesprin-2 indicating that NMIIA and NMIIB may interact with multiple isoforms of Nesprin-2. Confocal immunofluorescence microscopy and quantification of the images (Pearson's correlation coefficient mean value; NMIIA vs. Nesprin-2: 0.25; NMIIA vs. Nesprin-2: 0.30) depicted the

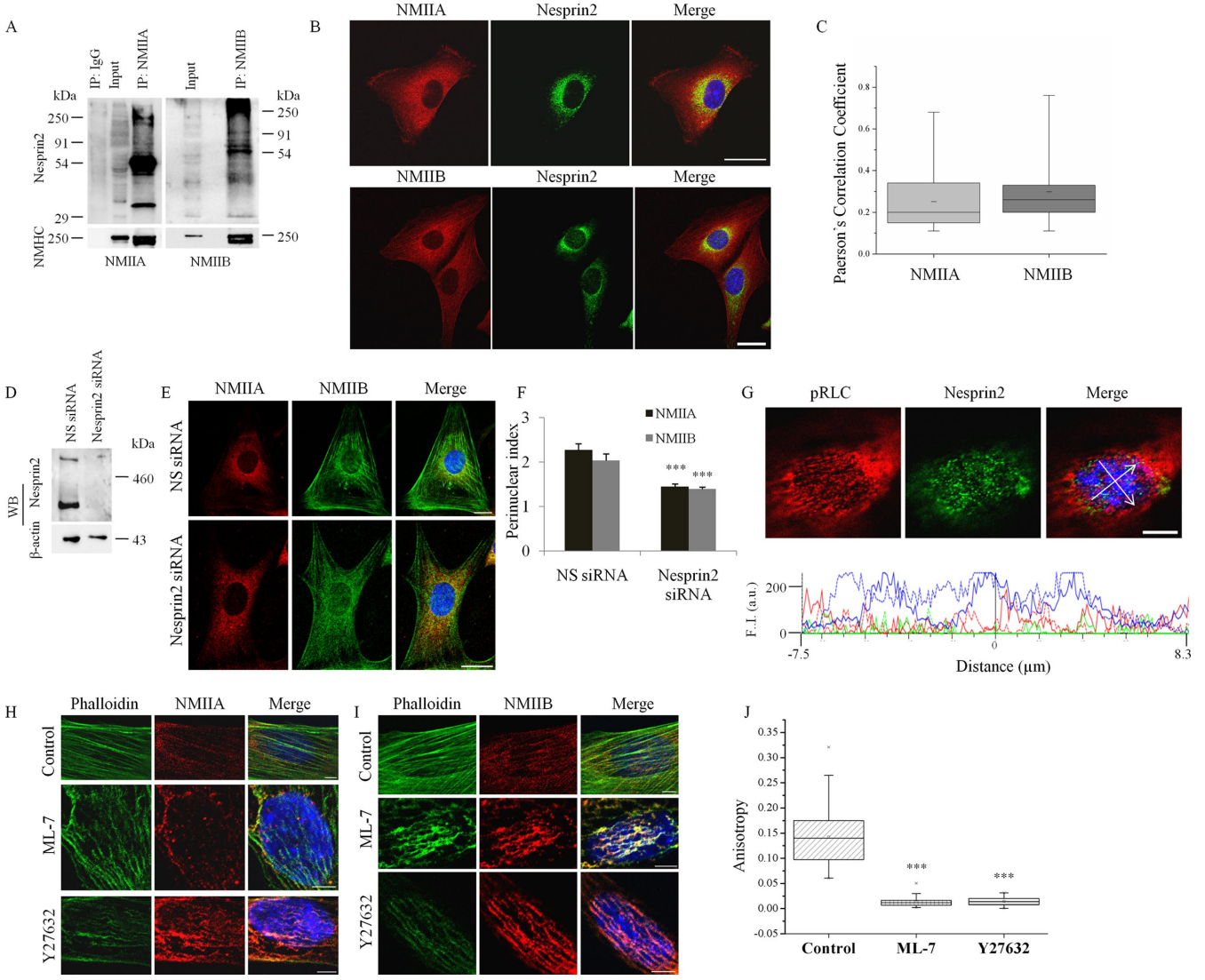

FIGURE 3: NMIIs interact with Nesprin-2 and assemble in the apical actin network. (A) Immunoprecipitates with anti-NMIIA or NMIIB antibodies were probed with antibody against Nesprin2. Immunoprecipitate with IgG served as a negative control. (B) Confocal microscopy of the primary cells coimmunostained with anti-Nesprin2 (green) and anti-NMIIA or -NMIIB (red) antibodies. (C) Box plots of Pearson's correlation coefficient of NMIIA or NMIIB with Nesprin2. (D) Immunoblots of NS or Nesprin2 siRNA–treated cell lysates probed with Nesprin2 or actin antibody. β-actin was used as loading control. (E) Confocal microscopy of NS or Nesprin2 siRNA–treated cells coimmunostained with anti-NMIIA (red) and -NMIIB (green) antibodies. (F) Quantification of perinuclear index of NMIIA and NMIIB ($n > 30$ cells from three independent experiments). (G) Confocal microscopy at the apical region of serum-starved and LPA-treated cells coimmunostained with anti-pRLC (red) and -Nesprin2 (green) antibodies. Intensity graphs of perpendicular lines are shown below. Localization of (H) NMIIA (red) and (I) NMIIB (red) at the apical actin cables across the nucleus stained with phalloidin (green) in serum-starved and LPA-treated cells in the presence or absence of ML-7 or Y27632. (J) Anisotropy of actin cables. $n > 60$ ROIs from two independent experiments. Scale bars: 25 μm (B), 20 μm (E), 10 μm (G), and 5 μm (H, I). ***, $P < 0.001$; NS vs. Nesprin2 siRNA; control vs. ML-7 or Y27632.

colocalization of NMIIA or NMIIB with Nesprin-2 at the perinuclear region (Figure 3, B and C). siRNA-mediated depletion of Nesprin-2 significantly reduced the perinuclear index of NMIIA (1.44 ± 0.06) and NMIIB (1.39 ± 0.04) as compared with NS siRNA–treated cells (NMIIA: 2.26 ± 0.14; NMIIB: 2.03 ± 0.15; Figure 3, D–F), suggesting Nesprin-2–dependent localization of NMIIs at the perinuclear area.

We next asked whether perinuclear NMIIA and NMIIB in the tumorigenic cells can assemble into the perinuclear actin network, which participates in transmembrane actin–associated nuclear (TAN) line or apical cap formation. Both TAN lines and apical actin caps are known to be involved in nuclear translocation and cellular mechanosensing (Gay *et al.*, 2011; Chang *et al.*, 2015). Under serum-starved and LPA (lysophosphatidic acid) stimulated condition, cells showed a prominent apical actin network (Supplemental Figure S4B, apical view), at which Nesprin2 (Figure 3G) and NMIIA and NMIIB (top panels of Figure 3, H and I) were localized. NMIIs were found to be mono- and diphosphorylated at this location (Supplemental Figure S4C). Treatment of cells with either ML-7 or Y27632 disorganized the NMIIA and NMIIB localization, which causes the disruption of the alignment of the apical actin network (Figure 3, H and I, middle and bottom panels). The anisotropy of apical actin fibers was measured, where 0 depicts no order

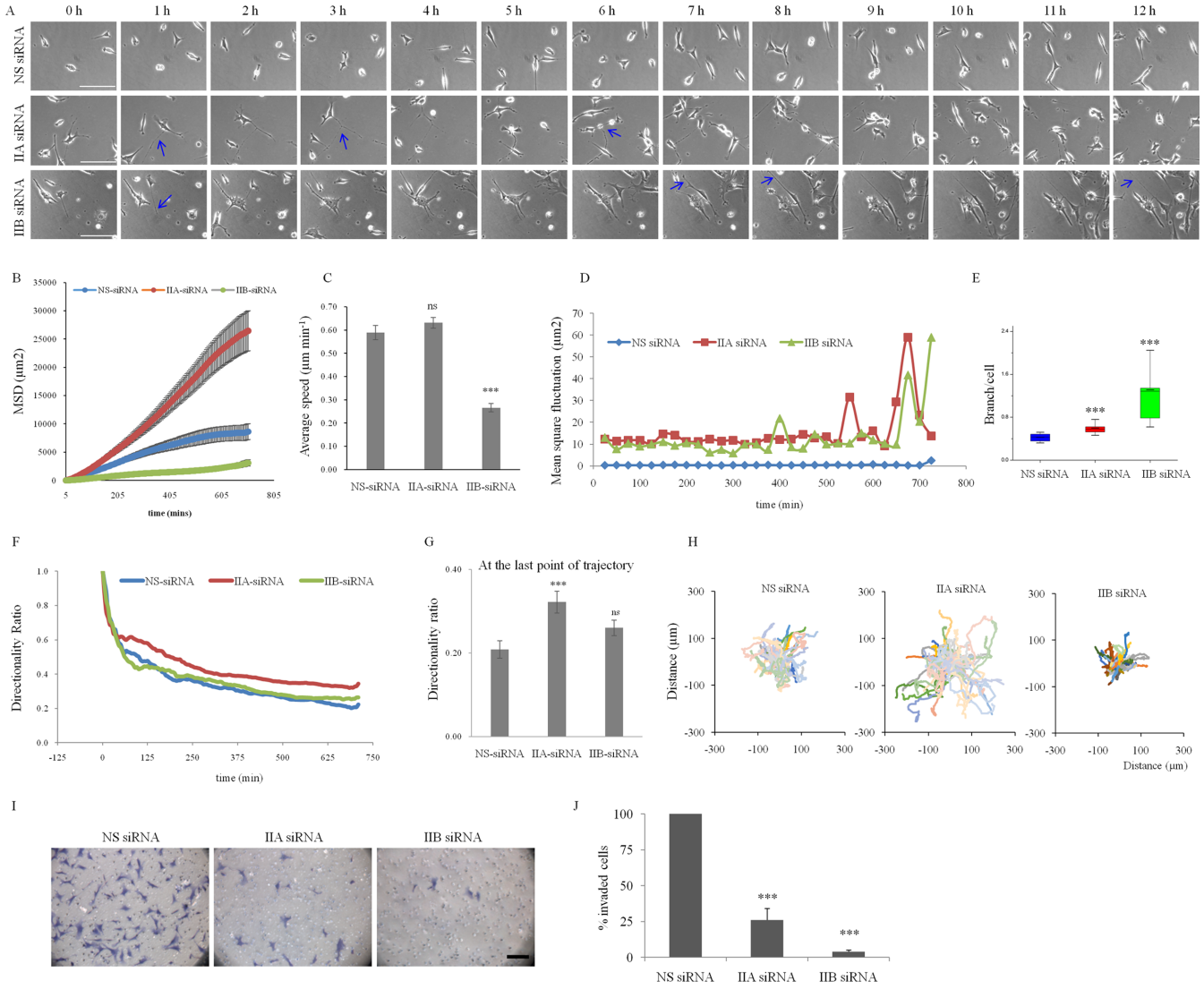

FIGURE 4: NMII knockdown cells show abnormal migration. (A) Time-lapse images of NS, IIA, or IIB siRNA–treated cells at indicated time points. Arrows indicate aberrant and/or branched protrusions. (B) MSD of cell body, (C) average speed of cells, (D) mean square fluctuation of protrusion length, (E) number of branches per cell at 12 h, (F) directionality ratio, (G) directionality ratio at 12 h, and (H) trajectories of cells were quantified (B–H; $n > 40$ cells from more than three experiments). (I) Bright-field images of NS, IIA, or IIB siRNA–treated cells stained with crystal violet. (J) Quantification of cell invasion ($n \geq 10$ fields from two independent experiments. Data are represented as mean ± SD). Scale bars: 100 μm (A) and 60 μm (I). ***, $P < 0.001$ NS vs. NMIIA or NMIIB siRNA; ns, not statistically significant.

(perfectly isotropic fibrils) and 1 indicates parallel fibrils (perfectly anisotropic). Control cells exhibited anisotropy 0.14 ± 0.008, whereas treatment of either ML-7 or Y27632 significantly decreased the anisotropy (ML-7: 0.013 ± 0.001 and Y27632: 0.014 ± 0.001; Figure 3J). Because ML7 or Y27632 treatment of cells resulted in a decrease in the anisotropy of the perinuclear actin fibers, it clearly indicated that NMIIs are important for maintaining the shape of the actin cap. Altogether, these data suggest that perinuclear NMIIA and NMIIB colocalize with the LINC protein Nesprin-2 and can assemble in the apical actin fibers. RLC phosphorylation is needed for uniform alignment of the apical actin network across the nucleus.

NMIIA- or NMIIB-depleted tumorigenic cells show abnormal migration patterns

Localization of NMIIA and NMIIB at the protrusive ends and perinuclear actin cables prompted us to check the two-dimensional cell migration and three-dimensional (3D) invasion of these cells. We performed time-lapse microscopy of nonspecific (NS) siRNA or siRNA specific to NMIIA- or NMIIB-treated cells to unravel the effect of NMII knockdown in tumor cell migration. Specificity of NMIIA or NMIIB siRNA was validated by immunoblot analysis (Supplemental Figure S5A). Figure 4A (top panel) and Supplemental Movie 1 show that NS siRNA–treated cells formed single or multiple filopodia and exhibited random movement. Filopodia attachment and detachment with substratum occurred both in and against the direction of protrusion growth. They were retracted back after the cell movement was completed. On the contrary, both IIA and IIB siRNA–treated cells lost randomness during migration. This was accompanied by abnormally long and branched filopodia. As the cells moved, part of the filopodia remained attached to the substratum and even pinched off from the cell (Figure 4A, middle and bottom panels, and Supplemental Movies 2 and 3). A delay in the disassembly of focal adhesion may contribute to a longer period of filopodia

attachment to the substratum during cell migration. Such abnormal protrusion dynamics was further evaluated by quantifying the average speed, Mean square displacement (MSD), cell directionality, and cell trajectory over a period of 12 h using DiPer software (Gorelik and Gautreau, 2014). Interestingly, IIA siRNA–treated cells showed increased MSD compared with NS or IIB siRNA–treated cells (Figure 4B). However, the speed of migration of IIA siRNA–treated cells remained almost unchanged (0.631 ± 0.023 μm min^{-1}), whereas IIB siRNA treatment resulted in significantly lower average migration speed (0.26 ± 0.017 μm min^{-1}) than NS siRNA–treated cells (0.589 ± 0.03 μm min^{-1}; Figure 4C). We further analyzed the filopodial defects seen in Figure 4A (middle and bottom panels). The mean square fluctuation of protrusion length over time depicted that NMIIA or NMIIB siRNA–treated cells show considerably high filopodial length fluctuation in comparison to NS siRNA (Figure 4D). Filopodia showed extensive branching in IIB siRNA (1.3 ± 0.16 branches per cell) compared with IIA siRNA (0.60 ± 0.03) or NS siRNA (0.42 ± 0.025)-treated cells (Figure 4E). Also, the lengths of the protrusions and their branches were found to be higher in IIA siRNA (54.15 ± 4.9 μm, 25.06 ± 1.79 μm) or IIB siRNA (45.81 ± 4.64 μm, 15.99 ± 0.92 μm)-treated cells in contrast to NS siRNA–treated cells (29.63 ± 3.0 μm, 7.8 ± 0.75 μm) as seen in the wound area of the wound-healing cell migration assay (Supplemental Figure S5, B–D). We found that NMIIA-knockdown cells exhibited a high directionality ratio over time (0.322 ± 0.05 at 12 h) compared with NS siRNA (0.208 ± 0.02) or IIB siRNA (0.26 ± 0.018; Figure 4, F and G), suggesting that the high directionality ratio of NMIIA-knockdown cells may result in high MSD as an effect of unidirectional movement, even though the speed of migration remained the same as NS siRNA–treated cells. This observation correlated with the higher spread area of the trajectory of NMIIA-knockdown cells as seen in Figure 4H. Note that NMIIB siRNA–treated cells displayed a lower spread area of the trajectory, which may be due to the significantly low average migration speed of these cells. As the invasiveness of a tumor cell is required for its tumorigenicity and is an effect of the migratory potential, we further tested the invasion ability of these cells in a 3D matrix. NMIIA- or NMIIB-knockdown cells showed an impaired ability to invade through matrigel set in a Boyden chamber. The number of invading cells was much lower in IIA siRNA (26.05 ± 8%) and IIB siRNA (3.88 ± 1.2%) as compared with NS-siRNA–treated cells (Figure 4, I and J). Altogether, these data suggest that NMIIA and NMIIB affect migration in a differential manner. Whereas NMIIA is involved in confining the area of movement, maintaining the dynamics of filopodia retraction, and facilitating cell randomness by preserving a low directional ratio, NMIIB, on the other hand, is involved in maintaining the speed of migration of the cells and filopodial branching.

NMIIA and NMIIB knockdown in tumorigenic cells results in alteration of gene expression

Recent reports suggest that nuclear envelope proteins are involved in regulation of gene expression by signal transmission from the cytoskeleton to the nucleus (Graham and Burridge, 2016; Kirby and Lammerding, 2018). The perinuclear enrichment of NMIIs, their localization at the actin cap, and coexistence with Nesprin-2 prompted us to examine whether NMIIA and NMIIB knockdown had any effect on the expression of genes involved in cancer progression. We screened the expression of a set of 84 cancer-related genes belonging to nine functionally diverse pathways, namely, cell cycle, apoptosis, cellular senescence, DNA damage and repair, metabolism, epithelial-to-mesenchymal transition (EMT), angiogenesis, hypoxia signaling, and telomere and telomerase using qRT-PCR array in NS, NMIIA, or NMIIB siRNA–treated primary cells. The specificity of siRNA against NMIIs was assessed by RT-PCR analysis and we find almost 70% down-regulation of NMIIA and NMIIB in knockdown conditions (Figure 5A). Scatter-plot and clustergram analysis showed that treatment of NMIIA and NMIIB siRNA displayed a change of greater than or equal to twofold expression of 12 and 15 out of 84 genes, respectively, which are involved in EMT, hypoxia, cellular senescence, and angiogenesis pathways (Supplemental Figure S6A). We selected four genes showing a greater than 10-fold change for further validation using semiquantitative PCR. We found that in the NMIIA silenced condition, there is a significant up-regulation of Tbx2. NMIIB knockdown resulted in a substantial down-regulation of Angpt1, Serpinb2, and Gsc (Supplemental Figure S6, A and B). Hierarchical clustering of these cancer pathway–related genes show differential expression in NMIIA and NMIIB-KD cells as compared with cells treated with NS siRNA (Figure 5B). Because gene expression levels emulate the joint effect of several underlying biological functions, specific networks (connection between the genes) may be involved in this. To explore the potential global effect of NMII knockdown in the cell-signaling pathways the gene expression data were examined using the ingenuity pathway analysis (IPA; Ingenuity Systems; www.ingenuity.com) to construct the probable pathways with the significantly induced genes (filtering through fold change >1.3 and P value < 0.05) to identify the specific canonical pathways associated with IIA siRNA and IIB siRNA–treated (knockdown) cells as done earlier (Ghosh *et al.*, 2015, 2018). In the gene ontology (GO) enrichment study for canonical pathway analysis, we chose to build the pathways connecting the top six networks, which were integrated into relevant networks computationally generated from the IPA knowledge base. The biological effects associated with IIA siRNA or IIB siRNA conditions are depicted in Figure 5, C and D, with the overlaying of canonical pathways (CPs). In both cases, death receptor signaling, apoptosis signaling, IL-8 signaling molecular mechanism of cancer, and telomere extension by telomerase are the top five CPs, which is highly significant (P value 2.99E-13–1.53E-08), but their molecules (having most connectivity in the networks) are different, such as Akt, ERK, ERK1/2, EGF2, P38, MAPK, and SRC (family) in IIA siRNA, and TNF, IL2, and IL-10 in IIB siRNA cells (Figure 5, C and D). This further delineates that the effect of NMIIA or NMIIB knockdown maybe exerted through different sets of genes during cancer progression.

NMIIs interact with Nesprin-2 and also colocalize at the perinuclear area (Figure 3). We were interested to know whether NMII-mediated gene regulation involved Nesprin-2 and contributed to cellular mechanoreciprocity. We had seen that Gsc and Serpinb2 were down-regulated in NMIIA- and NMIIB-KD cells (Supplemental Figure S6, A and B). In parallel, we found more than 90% down-regulation of Gsc and Serpinb2 in Nesprin-KD cells, similar to the NMIIB-KD condition (Figure 5E and Supplemental Figure S6C). These data provided an indication that NMIIs in the tumorigenic cells may be involved in LINC-mediated gene regulation. We further went on to ask whether NMIIA and NMIIB affected gene expression through mechanoresponsive pathways. Because the YAP/TAZ pathway is well known to be involved in mediating cellular mechanoresponses (Dupont *et al.*, 2011), we analyzed the impact of NMIIA- or NMIIB-KD by investigating the expression of CTGF (connective tissue growth factor), a YAP/TAZ target gene. The down-regulation of CTGF expression (more than 96%) in NMIIA- or NMIIB-KD condition further suggests that regulation of gene expression by NMIIs may be in a mechanoresponsive manner (Figure 5F). Altogether, the gene expression data suggest that NMIIA and NMIIB knockdown may affect cellular mechanoreciprocity of tumorigenic cells.

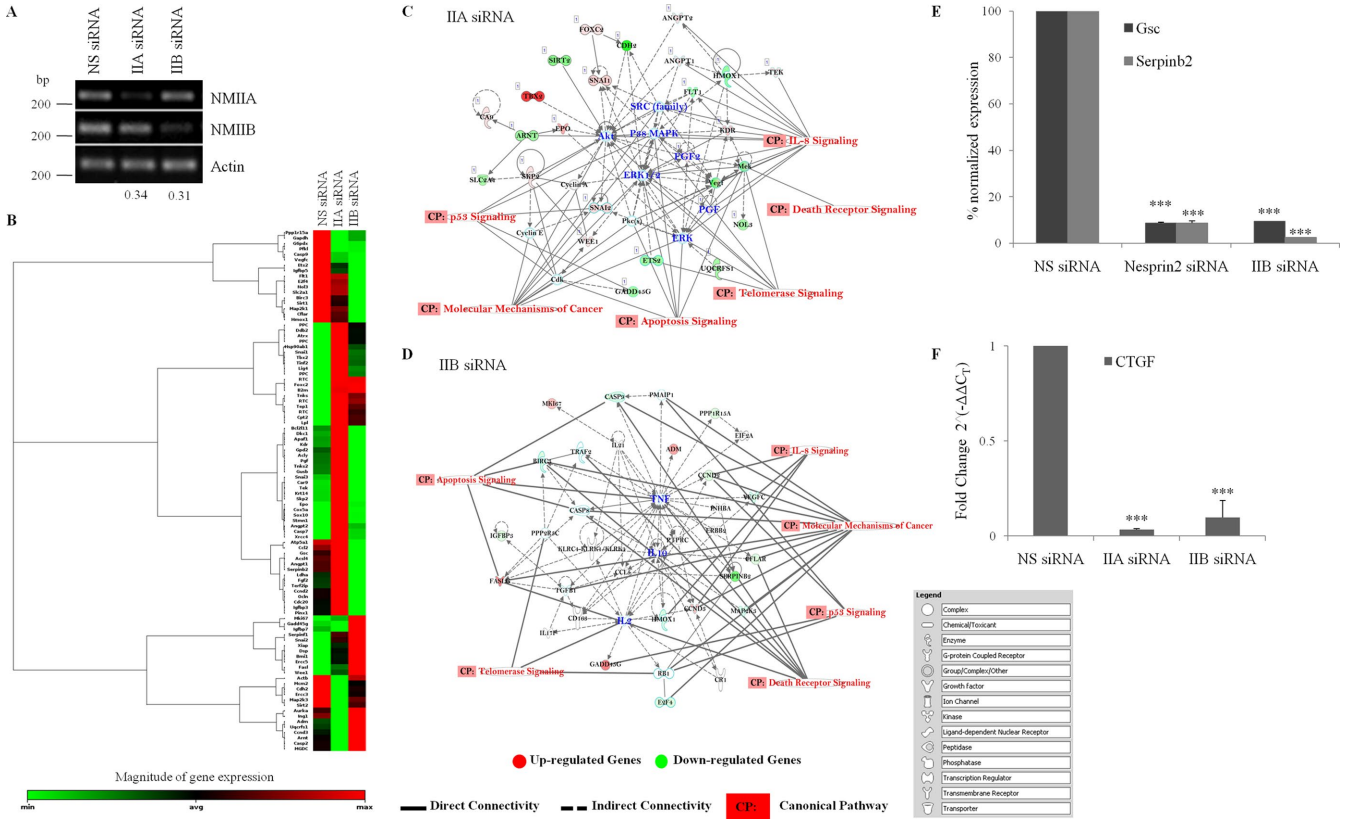

FIGURE 5: NMII knockdown cells show altered gene expression. (A) Down-regulation of mRNA of NMHC IIA and IIB in NMIIA and NMIIB siRNA–treated primary tumorigenic cells. (B) Unsupervised hierarchical clustering and heatmap analysis of the genes differentially expressed in cells treated with NS, IIA, or IIB siRNA. Gene expression is color-coded as Min (down-regulation) to Max (up-regulation). (C) IPA analysis of gene expression data. Connectivity of differentially expressed genes in the important signaling pathways in the IIA siRNA group or (D) the IIB siRNA group shown according to gene expression levels (≥1.33-fold change for IIA siRNA and ≥1.41-fold change for IIB siRNA; $P < 0.05$). Genes in the top networks (Network-1) were allowed to grow our pathway with the direct and indirect relationship from the IPA knowledge base. (E) Quantification of Gsc and Serpinb2 expression in NS, IIB, or Nesprin2 siRNA–treated cells using RT-PCR analysis, considering the relative intensity in a NS siRNA–treated sample as "100" (refer to Supplemental Figure S6 for a representative image). (F) Quantitative real-time PCR of CTGF expression in NS, IIA, or IIB siRNA–treated primary cells. $n = 3$; ***, $P < 0.001$ NS vs. NMIIA or NMIIB siRNA.

Knocking down of NMIIA and NMIIB reduces tumor growth in mice

We were interested to examine whether knockdown of NMIIA or NMIIB can affect colony growth in 3D or tumor growth in vivo in mice. We seeded the tumorigenic primary cells treated with NS, IIA, or IIB siRNA in agar and cultured them for 15 d. Supplemental Figure S8, A and B, shows that IIA or IIB knockdown can significantly decrease the colony area at days 7 and 15. Similarly, subcutaneous injection of siRNA-treated primary cells into male NOD/SCID mice resulted in lower tumor size (Supplemental Figure S8, C and D). To monitor how siRNA can affect tumor progression over time in vivo, we injected NMIIA or NMIIB siRNA at the site of tumor bulge formation and monitored the tumor growth at 48-h intervals (Figure 6A). Efficacy of the siRNA in vivo was tested by immunoblotting siRNA-treated tissue lysates (Supplemental Figure S8, E and F). Three representative images of tumors from each siRNA-treated tumor at 21, 29, and 31 d, respectively, are shown (Figure 6B). Note that a significant decrease in tumor size was observed in the presence of NMIIA or NMIIB siRNA compared with NS siRNA. We examined the histological characteristics of the siRNA-treated tumor tissues. Although some parts of the IIA or IIB siRNA–treated tissue were transformed, some parts still showed an orderly structure. In contrast, there was a complete loss of such tissue organization in the entire area of the NS-siRNA–treated section (Figure 6C). A comparison of the tumor volume and growth rate between NS siRNA, IIA siRNA, and IIB siRNA–treated tumors illustrates that IIA or IIB siRNA–treated tumors had lower volume compared with the NS siRNA–treated tumors. Although NS siRNA tumors required only 13 d to grow per cm^3 volume, IIA and IIB siRNA–treated mice required 20 and 38 d, respectively (Figure 6, D and E). Taken together, these data suggest that NMIIA and NMIIB are important for tumor progression.

DISCUSSION

How the cytoskeletal motor protein NMII may have vital roles in cancer progression other than cell division and migration is not well explored. In this study, we provide evidence that NMIIs colocalize at the perinuclear area and can act as a mechanotransducer during cancer progression.

Change in nuclear size and morphology mediated by nuclear envelope proteins including Nesprins may result in alteration of gene expression (Lammerding *et al.*, 2005; Isermann and Lammerding, 2013; Jevtic *et al.*, 2014). Nesprin-1 and -2 bind to cytoskeletal actin, whereas microtubule-associated motor proteins, kinesin and dynein, and the intermediate filament–associated protein, plectin, bind to

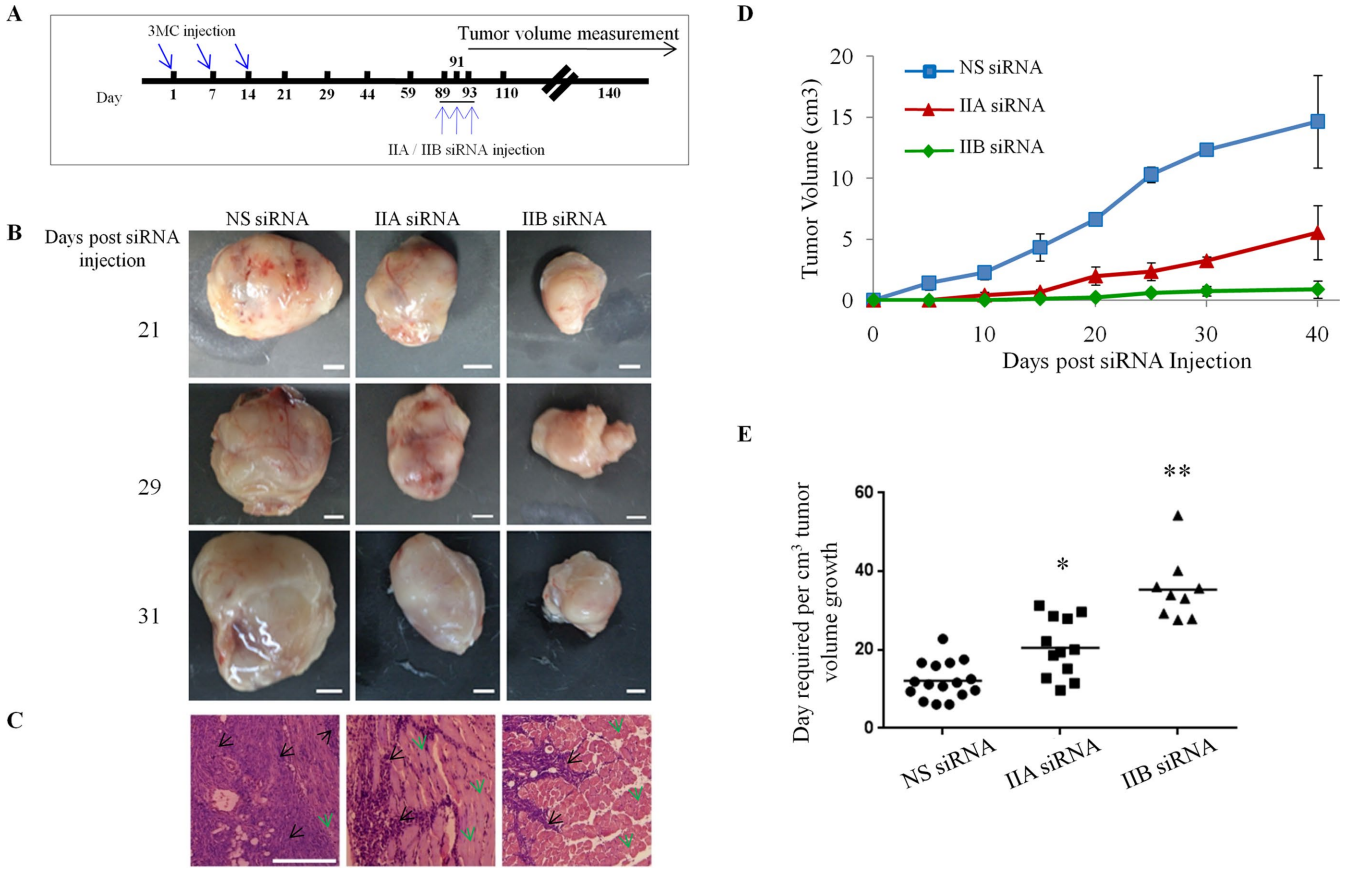

FIGURE 6: NMII knockdown reduces tumor growth. (A) Schedule of siRNA injection at the site of 3MC-induced tumor. (B) Images of tumor tissue at 21, 29, and 31 d post–NS, IIA, or IIB siRNA injection. (C) H&E staining of tumor tissue treated with NS, IIA, or IIB siRNA at 110 d. Green arrows indicate that cells were unable to transform in the presence of siRNA and black arrows indicate that cells were already transformed in the presence of 3MC. (D) Tumor volume and (E) number of days required to grow 1 cm^3 of tumor were calculated after siRNA injection. Scale bars: 5 mm (B) and 100 µm (C). *, $P < 0.05$ for NS vs. NMIIA siRNA; **, $P < 0.01$ for NS vs. NMIIB siRNA.

Nesprin-3 and -4, respectively, suggesting that cytosolic filament–associated proteins are integral components of the LINC complex and may be involved in transcriptional mechanoresponses (Rajgor and Shanahan, 2013; Jahed *et al.*, 2014; Graham and Burridge, 2016; Wang *et al.*, 2018). Initial work by Maniotis *et al.* (1997) provided some of the first evidence that forces can be transmitted from the cell surface to the nucleus through the cytoskeleton. Depletion or expression of dominant-negative Nesprin or SUN proteins severely impairs nucleo–cytoskeletal force transmission and magnitude of applied force correlated with the level of transcription (Lombardi *et al.*, 2011; Banerjee *et al.*, 2014). Here we show that NMIIs interact with Nesprin-2 in primary tumorigenic cells and are localized at the nuclear periphery (Figure 3, A–F), supporting the notion of actomyosin-mediated gene regulation through LINC. NMIIs localize not only at the perinuclear area but also at the stress fibers and protrusions (Figures 2 and 3). Multicompartment localization of proteins enhance their effect on intrinsic or extrinsic factors (Thul *et al.*, 2017), which suggests that NMIIs might have diverse protein–protein interactions and increased functionality in tumorigenic cells.

In normal cells, NMIIs are required for basic cellular functions such as cytokinesis, migration, etc. Knocking out of NMIIs in normal cells may lead to abnormal phenotypes through different mechanisms, such as SCC in skin or tongue. In one case, NMIIA plays a role in stabilizing p53 and its nuclear retention (Schramek *et al.*, 2014), whereas in the other case loss of NMIIA leads to failure in cytokinesis/karyokinesis (Anne Conti *et al.*, 2015) acting as a tumor suppressor in both cases. While the current article was in the review process, Georgouli *et al.* (2019) established that NMII drives tumor progression by reprogramming the innate immune microenvironment through immunomodulatory secretome. So, the mechanism may be different if NM IIs are knocked down in cancer cells. This indicates that up-regulation of NMIIs in cancerous cells may have different consequences on tumor growth. We previously reported that 3MC-induced tumors showed an increased amount of NMIIA and NMIIB, suggesting an increased amount of NMIIs or its activity in cancer cells may help tumor progression. In this study, we demonstrate that NMII can modulate gene expression through the LINC complex in 3MC-induced tumorigenic cells. Koebel *et al.* (2007) have shown that 3MC-induced tumors attain an equilibrium state by a host immune system. Altogether, these studies support a notion that tumor progression due to the reprogramming in cancer cells and/or cells present in the microenvironment may occur through NMII activity. Further study is needed to decipher whether NMII-mediated reprogramming is redundant or specific for tumor progression. Our system is also different from glioblastoma cells showing inadequate NMII activity that is restored on contractile activation by expression of constitutively active (CA)-RhoA, CA-ROCK1, or CA-MLCK (Wong *et al.*, 2015). This may not rule out the possibility of other effectors of Rho/ROCK that may participate in tumor regression on constitutive activation of the Rho/ROCK pathway, limiting the role of NMII in tumors. In contrast,

the tumor progression in 3MC-induced sarcoma tumors is rather associated with an increased NMII expression and more than 90% of isolated primary tumorigenic cells show NMIIA and NMIIB expression (Figure 1E). Unlike the previous works depicting the effect of NMII knockout in cancer development, our study decodes the role of NMII up-regulation in a tumor induced by a polyaromatic hydrocarbon carcinogen (3MC) that binds to the DNA forming a cancer-DNA phenotype (Malins *et al.*, 2004). This opens another window of possible perinuclear protein interactome, but at this stage we do not know the mutational landscape of these tumorigenic cells. Further work is warranted to decipher the standing of NMIIA or NMIIB in this context.

We hypothesized that the localization of NMIIs at the protrusion tips is essential for filopodia dynamics (Figure 4). Subsequently, we checked the actin cytoskeleton with respect to NMII localization at the filopodial tips and the perinuclear area. We found that short actin fibers form the perinuclear actin moiety in primary tumorigenic cells where NMIIA and NMIIB are enriched. It is well known that pharmacological inhibition of NMIIs can change the actin organization in the cell (Totsukawa *et al.*, 2000; Katoh *et al.*, 2001). ML-7 treatment in these cells resulted in increased ventral and dorsal stress fiber organization, and reduced actin bundles at the filopodial tips. However, ROCK inhibition does not affect the actin bundles around the nucleus or at the filopodial tip but reduces long ventral and dorsal actin filaments (Supplemental Figure S3, E and F). Unlike the NMII localizations found in other migratory cells such as MDA-MB-231, MEFs, or NIH-3T3 where NMIIs are found to be localized at the front, rear—albeit at differential amounts, cortex, and lamella/lamellipodia boundary junction (Betapudi *et al.*, 2006; Cai *et al.*, 2006; Jorrisch *et al.*, 2013), here in 3MC-induced tumorigenic cells NMIIs are enriched in the perinuclear area and filopodial tips. Filopodial tip and perinuclear NMII localizations regulating actin reorganization may affect migration quite differently upon deletion of NMII in these cells than reported previously. In addition, NMII enrichment in the perinuclear area may affect both nuclear translocation and mechano-coupled gene expression (Figures 3 and 5).

Under serum-starved conditions, cells show distinct NMII localization at the apical actin cap (Figure 3, F–H, and Supplemental Figure S4, B and C). Apical actin caps connect to the nucleus through LINC complexes and are essential for nuclear positioning during migration and maintaining nuclear shape and morphology (Khatau *et al.*, 2009; Maninova and Vomastek, 2016; Maninova *et al.*, 2017; Kirby and Lammerding, 2018). Interestingly, apical caps are attached to and regulated by the focal adhesion complex of the cells (Kim *et al.*, 2012), which indicates that they are involved in signal transduction from the extracellular matrix to the nucleus (Chambliss *et al.*, 2013; Jahed *et al.*, 2014). We uncover that both pRLC and ppRLC are present and colocalize at the apical actin cables (Supplemental Figure S4B), which may be regulated by MLCK and/or Rho/ROCK kinases (Figure 3, G–I). Diphosphorylation (ppRLC) promotes assembly and stability of NMII filaments in vitro (Iwasaki *et al.*, 2001; Vicente-Manzanares and Horwitz, 2010). As ppRLC augments the tension acting on the actomyosin stress fibers and polarity of migrating cells (Mizutani *et al.*, 2006), the presence of ppRLC in the apical cables is indicative of high MgATPase activity and more stability of NMIIA and NMIIB localized at the apical actin network. Because cancer progression is associated with extensive genetic reprogramming (Hanahan and Weinberg, 2011), perinuclear actin network–mediated nucleo–cytoskeletal signaling may be warranted for cellular reprogramming. We hypothesized that the high NMII activity in the apical cap not only facilitates nuclear positioning during migration but also enables efficient mechanotransduction contributing to the tumorigenicity of the cells. The reciprocity of cells and tumor microenvironment is the key step to cancer progression (Georgouli *et al.*, 2019). The hallmark of cancer progression is concurrent to the substantial cross-talk between different cellular signaling circuits. High ECM stiffness aggravates myofibroblast differentiation and potentiates expression of mechanoresponsive genes and cellular reprogramming of cancer cells (Hanahan and Weinberg, 2011; Quail and Joyce, 2013; Kirby and Lammerding, 2018). Myofibroblast or CAFs (cancer-associated fibroblasts) may not only augment but even initiate cancer (Goruppi and Dotto, 2013). In this study, we could detect cell proliferation and tissue transformation as early as 44–59 d (Figure 1, B–D) and tumorigenic myofibroblast cells isolated at 89 d show expression of NMIIA and NMIIB. Perinuclear localization of NMII in these cells gives us further indication that NMIIs may be involved in cellular reprogramming and mechanotransduction through interaction of NMIIs with the LINC complex proteins (Figures 3–5).

Tajik *et al.* (2016) established that activity of GFP-tagged DHLR transgene in CHO cells can be modulated by extracellular forces through integrins to the nuclear interior. Interestingly, Le *et al.* (2016) showed that Emerin enrichment at the nucleus correlates with the perinuclear enrichment of NMIIA, providing tensile strength to the F-actin structure at the ONM under biaxial cyclic mechanical strain in human epidermal progenitor cells (EPCs). We find that knockdown of NMIIB shows down-regulation of Gsc, Ang1, and Serpinb2 (Supplemental Figure S6, B and C), involved in promoting EMT, angiogenesis, and maintaining senescence, respectively (Hayes *et al.*, 2000; Hartwell *et al.*, 2006; Hsieh *et al.*, 2017). Interestingly, Nesprin-2–knockdown cells also show down-regulation of Gsc and Serpinb2 (Figure 5E), which is strikingly similar to expression of these genes in NMIIB-knockdown condition, reemphasizing the notion that an external signal from the tumor microenvironment may pass from the perinuclear actomyosin through the LINC complex to the nuclear interior.

Several biological processes, including embryogenesis, development, and tissue homeostasis, depend on the cellular ability to sense and respond to mechanical forces. Although it is known that mechanical forces can influence cell morphology and behavior, dissecting the molecular pathways that may be involved in generating transcriptional mechanoresponses and how inhibition of these pathways can give rise to diseased conditions may provide a future direction (Shao *et al.*, 2015; Kirby and Lammerding, 2018). The mechanism of development of human diseases associated with NMII mutations remains to be explored. Our IPA analysis predicts that many of the signaling pathways involved in physiological system development, disease development, and vital cellular and molecular functions are modulated by NMIIs (Supplemental Figure S7). We observed reduced tumor growth under NMIIA- or NMIIB-knockdown conditions (Figure 6). This may be due to the disruption of actomyosin-mediated cell-signaling networks that facilitate cancer progression. Our IPA analysis predicts that different regulators are influenced by NMIIA and NMIIB. Likewise, NMIIs may act as a signaling scaffold by transmitting intra- and extracellular signals through the LINC complex via different CPs (Figure 5B), or by nuclear envelope tethering (Keeling *et al.*, 2017) in the cancer cell. On the other hand, several reports documented that NMIIA localization and filament assembly can be modulated by interaction with other proteins such as S100A4 (Li and Bresnick, 2006), Lgl1 (Dahan *et al.*, 2012), MYBPH (Hosono *et al.*, 2012), UNC-45 (Lehtimaki *et al.*, 2017), integrin (Rosado *et al.*, 2011), spectrin (Smith *et al.*, 2018), Myo 18A (Billington *et al.*, 2015), and tropomyosin (Barua *et al.*, 2014). How these interactions can moderate the assembly and

function of NMII in the context of mechanotransduction remains to be explored. Regulation of NMII assembly at the perinuclear localization, filopodial tips, or at other subcellular areas may influence the level of mechanotransduction, and its understanding provides a therapeutic strategy for future study.

MATERIAL AND METHODS

Animal experiments

All mice were maintained according to the guidelines of the Institutional Animal Ethics Committee. A 3MC (Sigma-Aldrich, MO)-induced tumor was generated in 2-wk-old female Swiss albino mice according to the previous protocol (Saha *et al.*, 2011). Olive oil was used in vehicle-injected mice as a placebo control. The 3MC regime consisted of three doses (10 mg/kg body weight per dose) at an interval of 1 wk each. Tumor bulge was visible in mice within 80–100 d. To examine the effect of NMII knockdown, 5 µg of IIA or IIB siRNA in OptiMEM (Thermo Fisher Scientific, MA) was injected twice with an interval of 48 h with Lipofectamine 2000 (Thermo Fisher) at the site of the tumor on day 89 (time point when the majority of the mice show the tumor bulge). Tumor tissue was collected 72 h post–second dose and siRNA efficacy was analyzed by immunoblot analyses. The volume of the NS, IIA, or IIB siRNA–treated 3MC-induced tumor was measured using a digital slide caliper every 48 h post–siRNA injection up to 40 d. Tumor volume was calculated using the modified ellipsoid formula (1/2 × length × width^2; Kajiwara *et al.*, 2018).

Immunohistochemistry and immunofluorescence

Tissues from the site of injection or the tumor tissues were fixed in 10% Formalin solution overnight. Paraffin-embedded tissue sections were prepared for immunohistochemistry and immunofluorescence (Saha *et al.*, 2011). Briefly, deparaffinized and rehydrated sections were subjected to antigen retrieval in 10 mM sodium citrate (pH 6) for 20 min at 80°C. Sections were then permeabilized with 0.1% Triton X-100 and blocked in normal goat serum followed by incubation with primary antibody against PCNA (Santa Cruz Biotechnology, TX), NMIIA (Covance or Abcam, Cambridge, UK), NMIIB, (Covance or Abcam), α-SMA (Sigma-Aldrich), CD34, and Vimentin (Cell Signaling). PCNA was visualized by a mouse-specific HRP (horseradish peroxidase)/DAB (ABC) Detection IHC Kit (Abcam) following the manufacturer's protocol, and others by indirect immunofluorescence analysis in which secondary antibody conjugated to Alexa Fluor 488, 594, or 546 (Thermo Fisher) was used for visualization. Morphological assessment of the analogous tissue sections was carried out using hematoxylin and eosin stains.

Similarly, isolated primary tumorigenic cells were washed in phosphate-buffered saline (PBS) and fixed in 4% paraformaldehyde for 20 min, permeabilized with 0.5% Triton X-100 for 10 min, and blocked with goat serum (Santa Cruz) for 60 min. Cells were incubated with Desmin (Santa Cruz), Nesprin-2 (Abcam), pRLC, ppRLC (Cell Signaling) or previously mentioned primary antibodies at 4°C overnight followed by mouse or rabbit secondary antibody conjugated to Alexa Fluor 488, 594, or 546 (Thermo Fisher) incubation for 1 h. DAPI was used to stain the nucleus and actin filaments were visualized with Alexa 488-Phalloidin. Coverslips were mounted using Vectamount (Vector Laboratories, USA) or Prolong gold antifade reagent (Thermo Fisher). Images were captured using Nikon Ti-E C1 equipped with NIS-AR software (Nikon, Japan), Carl Zeiss LSM880 confocal microscope (Zeiss, Germany) equipped with Zen Blue software or Leica TCS SP8 confocal laser-scanning microscope equipped with Leica software (Leica, Wetzler, Germany).

Primary cell culture, drug treatment and siRNA transfection

Isolation of primary cells from tumor tissue was carried out following the published protocols (Mitra *et al.*, 2013). Briefly, 89–95 d 3MC-induced tumor tissues isolated from mice were minced, and washed with Hank's balanced salt solution (HBSS). Minced tissue was treated for 1–2 h with 0.1% Collagenase IV (Thermo Fisher) to obtain cell suspension. Cells were pelleted, washed with HBSS, plated in collagen-coated dishes and maintained up to 20 passages in DMEM supplemented with 10% fetal bovine serum (FBS), penicillin, and streptomycin (Thermo Fisher), in a humidified incubator at 37°C supplied with 5% CO_2. Cell suspensions were cryopreserved for future experiments. All experiments were carried out between passages 2–10. For siRNA transfection, 30–60 picomole siRNA was transfected using Lipofectamine RNAimax (Thermo Fisher) according to manufacturer's protocol. NMIIA siRNA 1(Myh9): sense 5′GCUACAUUGUUGGUGCCAA [dT][dT]3′ and antisense 5′ UUGGCACCAACAAUGUAGC [dT][dT] 3′, or NMIIA siRNA 2: sense 5′ GUCAUCAACCCUUAUAAGA [dT][dT] 3′ and antisense 5′UCUUAUAAGGGUUGAUGAC [dT][dT]3′, NMIIB siRNA1 (Myh10): siRNA pool EMU068341, or NMIIB siRNA2: sense 5′GCCAUAUCAGAGUCUGCUU [dT][dT]3′ and antisense 5′AAGCAGACUCUGAUAUGGC [dT][dT]3′ were procured from Sigma-Aldrich, and Nesprin2 siRNA (Syne2): Accell siRNA pool E-056764-00-0005 from GE Healthcare, USA. Cells were analyzed 24–72 h after transfection. To determine the perinuclear index, Bezier ROI (region of interest)-1 was constructed around the rim of the nucleus (perinuclear) and ROI-2 encompassing the whole cell. Fluorescence intensity (F.I.) per µm^2 was measured in the given ROIs. Ratio of F.I. per µm^2 of ROI-1 to F.I. per µm^2 of ROI-2 was considered as perinuclear index. Similarly, filopodial tip index was calculated as ratio of F.I at tip (ROI 1) per µm^2 and F.I at whole filopodia (ROI 2) per µm^2 using NIS-AR software. For drug-treated experiments, cells were treated with 30 µM ML-7 or Y27632 for 1 h. Both siRNA and drug-treated cells were fixed and immunostained as mentioned before. To visualize the perinuclear actin network, cells were serum starved for 2 d followed by 10 µM LPA (Santa Cruz) treatment for 1 h and then subjected to immunofluorescence as before (Luxton *et al.*, 2010). Anisotropy was measured using Fibril plugin in ImageJ software. ROI was selected from the apical actin network across the nucleus as published previously (Boudaoud *et al.*, 2014).

Flow cytometry

Primary cells were washed in PBS and fixed overnight at 4°C by adding cell suspension dropwise to 70% ethanol (Merck). On day 2, cells were washed, resuspended in PBS containing 1% bovine serum albumin (BSA; Merck Milipore), 10% goat serum (Merck Milipore), and costained for combinations of any two: NMIIA (Covance, Abcam), NMIIB, CD34 (Abcam), α-SMA (Sigma), and Vimentin (Cell Signaling Technology). After 2 h incubation, cells were washed with PBS (2000 rpm, 5 min) and incubated in 500 µl PBS solution containing Alexa Fluor 647 and 488 (Thermo) for 1–2 h. Cells were then washed, resuspended in FACS flow buffer, and immediately acquired on a BD FACSAria III flow cytometer (BD Biosciences). Data were analyzed using BD FACSDiva v8.0 software.

Time-lapse video microscopy

Cells isolated from the 3MC-induced tumor were seeded on collagen-coated dishes. Time-lapse movies of the cells treated with NS, IIA, or IIB siRNA were acquired by capturing images at 5-min intervals for 12 h using a CCD camera (Digital Sight DS-Qi1MC, Nikon) in a live cell incubator at 37°C supplied with 5% CO_2. Movies were played at a speed of 10 frames per second. The center of each cell

in the image sequence was manually tracked by ImageJ (National Institutes of Health). Cell trajectory, MSD, directional persistence, and average speed were calculated using previously published protocol, DiPer software (Gorelik and Gautreau, 2014). Mean square fluctuation at each time point was calculated as the square of the average change in protrusion length (μm) between consecutive time points for 12 h, and branching per cell was calculated by the formula (number of branches in a field/number of cells in the given field).

3D invasion

Cell migration through a Boyden chamber (Corning) was performed using the manufacturer's protocol. Briefly, 2.5×10^5 primary cells were plated in each well of 24-well transwell plates containing inserts (Corning) in FBS-free medium. The medium below the insert was supplemented with 10% FBS. The setup was kept at 37°C overnight at 5% CO_2 conditions in a humidified incubator. On day 2, the cell inserts were fixed with methanol for 20 min, washed in PBS, and stained with crystal violet (Sigma-Aldrich) for 15 min. Images were captured using a bright-field microscope (Leica). The number of invaded cells per field was counted using the ImageJ cell counter.

Protein analysis

Extracts of primary cells and tumor tissues were prepared in an extraction buffer composed of 50 mM Tris-HCl (pH 8.0), 60 mM KCl, 10 mM $MgCl_2$, 5 mM ATP, 4 mM EDTA, 1 mM dithiothreitol, 1% Nonidet P-40, 0.5 mM phenylmethylsulfonyl fluoride, and protease inhibitors cocktail and RIPA buffer, respectively, at 4°C. Cell lysates were sedimented at 10,000 × *g* for 10 min. NMIIA and NMIIB were immunoprecipitated with antibody specific to NMHCIIA (Abcam) and NMHCIIB (Covance), respectively, using SureBeads Protein G Magnetic Beads (Bio-Rad, CA) as per the manufacturer's protocol. Immunoglobulin G (IgG) was used as negative control for immunoprecipitation. Immunoprecipitates, cell or tumor tissue lysates were fractionated by SDS–PAGE on 8% or 10% polyacrylamide Tris-glycine gels, and transferred onto 0.45 μm polyvinylidene difluoride membranes (Millipore) as previously published (Saha *et al.*, 2011; Das *et al.*, 2015). Membranes were blocked with 5% BSA or nonfat milk (Sigma-Aldrich) and incubated overnight at 4°C with primary antibodies specific to NMIIA, NMIIB, α-tubulin, β-actin (Sigma-Aldrich), Nesprin-2 (Abcam), or GAPDH (Santa Cruz). Membranes were then incubated with HRP-conjugated secondary antibody (Thermo Fisher) for 2 h. Chemiluminescence signal was visualized by Super Signal Femto Reagent (Thermo Fisher) and captured using a ChemiDoc Touch Imaging system (Bio-Rad).

RNA isolation and gene expression analysis

Total RNA from NS, IIA, or IIB siRNA–treated primary cells was isolated using a RNeasy mini kit (Qiagen, Limburg, Netherlands). The total RNA from three independent biological samples was pooled and reverse transcribed with an RT2 First Strand Kit (Qiagen) according to the manufacturer's protocol (Haidet-Phillips *et al.*, 2011). Real-time quantitative PCRs were carried out using RT2 Real-Time SYBR Green/Rox PCR Master Mix (Qiagen), and PCR arrays (Cancer PathwayFinder RT2 Profiler PCR Array) were run on an ABI 7500 fast block. Array data were analyzed using the web-based PCR Array Data Analysis Software available on the Qiagen website. Gene expression was normalized using a set of five housekeeping genes and fold regulation was used to analyze changes in gene expression as per manufacturer's instructions. In the case of CTGF, relative fold change in gene expression was calculated using the $\Delta\Delta C_T$ method. GAPDH was used as housekeeping control and NS siRNA was treated as the reference sample set. All primer sequences are listed in the Supplemental Materials and Methods.

IPA

We engaged the information in the Ingenuity Knowledge Base (Genes Only) as a reference set that considers both direct and indirect relationships as done previously (Ghosh *et al.*, 2015, 2018). We used the data sources from ingenuity expert findings and the "Core Analysis" function to interpret the data in the perspective of biological processes, pathways, and networks. Data sets from the RT-PCR differential gene expression containing gene identifiers and corresponding expression values were uploaded into the application and mapped to its corresponding gene object in the Ingenuity Pathways Knowledge Base. Genes differentially expressed with $P < 0.05$ were overlaid onto global molecular networks, developed from information contained in the knowledge base. Networks were then algorithmically generated based on their connectivity. Canonical pathway analysis was used to identify function-specific genes that are significantly present within the networks. Biofunction analysis identifies the associations between the data set and the information in the IPA library. This association was then calculated from the ratio of the number of genes from the data set that are associated with the biofunctions divided by the total number of molecules that are associated with the function. The probability that each biological function and/or disease assigned to that data set are due to chance alone and were calculated using a right-tailed Fisher's exact test (in built). Overrepresentation of the molecules in a given process was considered to be statistically significant when $P < 0.05$. The overrepresented functional or pathway processes are those which have more focus molecules than expected by chance. Using a pathway approach, we capitalize on the prior biological knowledge about genes and pathways that may be affected by NMII expression during tumor progression.

Statistical analysis

Differences among NS, IIA, and IIB siRNA–treated cells in the various parameters like length, speed, number of cells, and fluorescence intensity were assessed using the Student *t* tests and one-way analysis of variance. Data are represented as mean ± SEM or mean ± SD. Statistical analyses were performed using GraphPad. Differences were considered to be significant if the *P* value was ≤0.05.

ACKNOWLEDGMENTS

We acknowledge Surajit Sinha, Partha Sarathi Dastidar, Mahua R. Das, Provas Das, Kumarjeet Banerjee, and Kaushik Das from the Indian Association for the Cultivation of Science (IACS) and Malancha Ta and Umesh Goyal from Indian Institute of Science Education and Research, Kolkata, for technical support. We thank all other laboratory members for reading the manuscript and providing valuable comments. We acknowledge the Department of Biotechnology (DBT), Government of India (BT/PR12910/BRB/10/1389/2015 to S.S.J.), the Technical Research Center, IACS, a Wellcome Trust/DBT India Alliance Intermediate Fellowship (IA/I/13/1/500888 to Benu Brata Das), and the National Institute on Minority Health and Health Disparities (5G12MD007597-25 to S.G.) for funding and IACS for a fellowship to D.H.

REFERENCES

Aguilar-Cuenca R, Juanes-Garcia A, Vicente-Manzanares M (2014). Myosin II in mechanotransduction: master and commander of cell migration, morphogenesis, and cancer. Cell Mol Life Sci 71, 479–492.

Anne Conti M, Saleh AD, Brinster LR, Cheng H, Chen Z, Cornelius S, Liu C, Ma X, Van Waes C, Adelstein RS (2015). Conditional deletion of

nonmuscle myosin II-A in mouse tongue epithelium results in squamous cell carcinoma. Sci Rep 5, 14068.
Banerjee I, Zhang J, Moore-Morris T, Pfeiffer E, Buchholz KS, Liu A, Ouyang K, Stroud MJ, Gerace L, Evans SM, *et al.* (2014). Targeted ablation of Nesprin 1 and Nesprin 2 from murine myocardium results in cardiomyopathy, altered nuclear morphology and inhibition of the biomechanical gene response. PLoS Genet 10, e1004114.
Barua B, Nagy A, Sellers JR, Hitchcock-DeGregori SE (2014). Regulation of nonmuscle myosin II by tropomyosin. Biochemistry 53, 4015–4024.
Beach JR, Bruun KS, Shao L, Li D, Swider Z, Remmert K, Zhang Y, Conti MA, Adelstein RS, Rusan NM, *et al.* (2017). Actin dynamics and competition for myosin monomer govern the sequential amplification of myosin filaments. Nat Cell Biol 19, 85–93.
Betapudi V, Licate LS, Egelhoff TT (2006). Distinct roles of nonmuscle myosin II isoforms in the regulation of MDA-MB-231 breast cancer cell spreading and migration. Cancer Res 66, 4725–4733.
Billington N, Beach JR, Heissler SM, Remmert K, Guzik-Lendrum S, Nagy A, Takagi Y, Shao L, Li D, Yang Y, *et al.* (2015). Myosin 18A coassembles with nonmuscle myosin 2 to form mixed bipolar filaments. Curr Biol 25, 942–948.
Boudaoud A, Burian A, Borowska-Wykret D, Uyttewaal M, Wrzalik R, Kwiatkowska D, Hamant O (2014). FibrilTool, an ImageJ plug-in to quantify fibrillar structures in raw microscopy images. Nat Protoc 9, 457–463.
Cai Y, Biais N, Giannone G, Tanase M, Jiang G, Hofman JM, Wiggins CH, Silberzan P, Buguin A, Ladoux B, Sheetz MP (2006). Nonmuscle myosin IIA-dependent force inhibits cell spreading and drives F-actin flow. Biophys J 91, 3907–3920.
Chambliss AB, Khatau SB, Erdenberger N, Robinson DK, Hodzic D, Longmore GD, Wirtz D (2013). The LINC-anchored actin cap connects the extracellular milieu to the nucleus for ultrafast mechanotransduction. Sci Rep 3, 1087.
Chang W, Worman HJ, Gundersen GG (2015). Accessorizing and anchoring the LINC complex for multifunctionality. J Cell Biol 208, 11–22.
Coluccio LM (ed.) (2008). Myosins; A Superfamily of Molecular Motors. In: Proteins and Cell Regulation, Vol. 7, Dordrecht, Netherlands, Springer.
Conti MA, Adelstein RS (2008). Nonmuscle myosin II moves in new directions. J Cell Sci 121, 11–18.
Crisp M, Liu Q, Roux K, Rattner JB, Shanahan C, Burke B, Stahl PD, Hodzic D (2006). Coupling of the nucleus and cytoplasm: role of the LINC complex. J Cell Biol 172, 41–53.
Dahan I, Yearim A, Touboul Y, Ravid S (2012). The tumor suppressor Lgl1 regulates NMII-A cellular distribution and focal adhesion morphology to optimize cell migration. Mol Biol Cell 23, 591–601.
Das P, Saha S, Dey SK, Das MR, Jana SS, Chandra S, Sarkar DP, Das A, Sen S (2015). Phosphorylation of nonmuscle myosin II-A regulatory light chain resists Sendai virus fusion with host cells. Sci Rep 5, 10395.
Dey SK, Singh RK, Chattoraj S, Saha S, Das A, Bhattacharyya K, Sengupta K, Sen S, Jana SS (2017). Differential role of nonmuscle myosin II isoforms during blebbing of MCF-7 cells. Mol Biol Cell 28, 1034–1042.
Dupont S, Morsut L, Aragona M, Enzo E, Giulitti S, Cordenonsi M, Zanconato F, Le Digabel J, Forcato M, Bicciato S, *et al.* (2011). Role of YAP/TAZ in mechanotransduction. Nature 474, 179–183.
Gay O, Gilquin B, Nakamura F, Jenkins ZA, McCartney R, Krakow D, Deshiere A, Assard N, Hartwig JH, Robertson SP, Baudier J (2011). RefilinB (FAM101B) targets FilaminA to organize perinuclear actin networks and regulates nuclear shape. Proc Natl Acad Sci USA 108, 11464–11469.
Georgouli M, Herraiz C, Crosas-Molist E, Fanshawe B, Maiques O, Perdrix A, Pandya P, Rodriguez-Hernandez I, Ilieva KM, Cantelli G, *et al.* (2019). Regional activation of myosin II in cancer cells drives tumor progression via a secretory cross-talk with the immune microenvironment. Cell 176, 757–774.
Ghosh S, Loffredo CA, Mitra PS, Trnovec T, Palkovicova Murinova L, Sovcikova E, Hoffman EP, Makambi KH, Dutta SK (2018). PCB exposure and potential future cancer incidence in Slovak children: an assessment from molecular finger printing by Ingenuity Pathway Analysis (IPA) derived from experimental and epidemiological investigations. Environ Sci Pollut Res 25, 16493–16507.
Ghosh S, Mitra PS, Loffredo CA, Trnovec T, Murinova L, Sovcikova E, Ghimbovschi S, Zang S, Hoffman EP, Dutta SK (2015). Transcriptional profiling and biological pathway analysis of human equivalence PCB exposure in vitro: indicator of disease and disorder development in humans. Environ Res 138, 202–216.
Gorelik R, Gautreau A (2014). Quantitative and unbiased analysis of directional persistence in cell migration. Nat Protoc 9, 1931–1943.
Goruppi S, Dotto GP (2013). Mesenchymal stroma: primary determinant and therapeutic target for epithelial cancer. Trends Cell Biol 23, 593–602.
Graham DM, Burridge K (2016). Mechanotransduction and nuclear function. Curr Opin Cell Biol 40, 98–105.
Haidet-Phillips AM, Hester ME, Miranda CJ, Meyer K, Braun L, Frakes A, Song SW, Likhite S, Murtha MJ, Foust KD, *et al.* (2011). Astrocytes from familial and sporadic ALS patients are toxic to motor neurons. Nat Biotechnol 29, 824–828.
Hanahan D, Weinberg RA (2011). Hallmarks of cancer: the next generation. Cell 144, 646–674.
Hartwell KA, Muir B, Reinhardt F, Carpenter AE, Sgroi DC, Weinberg RA (2006). The Spemann organizer gene, Goosecoid, promotes tumor metastasis. Proc Natl Acad Sci USA 103, 18969–18974.
Hayes AJ, Huang WQ, Yu J, Maisonpierre PC, Liu A, Kern FG, Lippman ME, McLeskey SW, Li LY (2000). Expression and function of angiopoietin-1 in breast cancer. Br J Cancer 83, 1154–1160.
Hosono Y, Usukura J, Yamaguchi T, Yanagisawa K, Suzuki M, Takahashi T (2012). MYBPH inhibits NM IIA assembly via direct interaction with NMHC IIA and reduces cell motility. Biochem Biophys Res Commun 428, 173–178.
Hsieh H-H, Chen Y-C, Jhan J-R, Lin J-J (2017). The serine protease inhibitor serpinB2 binds and stabilizes p21 in senescent cells. J Cell Sci 130, 3272–3281.
Isermann P, Lammerding J (2013). Nuclear mechanics and mechanotransduction in health and disease. Curr Biol 23, R1113–R1121.
Iwasaki T, Murata-Hori M, Ishitobi S, Hosoya H (2001). Diphosphorylated MRLC is required for organization of stress fibers in interphase cells and the contractile ring in dividing cells. Cell Struct Funct 26, 677–683.
Jahed Z, Shams H, Mehrbod M, Mofrad MRK (2014). Mechanotransduction pathways linking the extracellular matrix to the nucleus. Int Rev Cell Mol Biol 310, 171–220.
Jevtic P, Edens LJ, Vukovic LD, Levy DL (2014). Sizing and shaping the nucleus: mechanisms and significance. Curr Opin Cell Biol 28, 16–27.
Jorrisch MH, Shih W, Yamada S (2013). Myosin IIA deficient cells migrate efficiently despite reduced traction forces at cell periphery. Biol Open 2, 368–372.
Kajiwara C, Fumoto K, Kimura H, Asano K, Kikuchi A, Nojima S, Morii E, Odagiri K, Yamasaki M, Doki Y, *et al.* (2018). p63-Dependent Dickkopf3 expression promotes esophageal cancer cell proliferation via CKAP4. Cancer Res 78, 6107–6120.
Kassianidou E, Hughes JH, Kumar S (2017). Activation of ROCK and MLCK tunes regional stress fiber formation and mechanics via preferential myosin light chain phosphorylation. Mol Biol Cell 28, 3832–3843.
Katoh K, Kano Y, Amano M, Kaibuchi K, Fujiwara K (2001). Stress fiber organization regulated by MLCK and Rho-kinase in cultured human fibroblasts. Am J Physiol 280, C1669–C1679.
Keeling MC, Flores LR, Dodhy AH, Murray ER, Gavara N (2017). Actomyosin and vimentin cytoskeletal networks regulate nuclear shape, mechanics and chromatin organization. Sci Rep 7, 1–14.
Khatau SB, Hale CM, Stewart-Hutchinson PJ, Patel MS, Stewart CL, Searson PC, Hodzic D, Wirtz D (2009). A perinuclear actin cap regulates nuclear shape. Proc Natl Acad Sci USA 106, 19017–19022.
Kim D-H, Khatau SB, Feng Y, Walcott S, Sun SX, Longmore GD, Wirtz D (2012). Actin cap associated focal adhesions and their distinct role in cellular mechanosensing. Sci Rep 2, 555.
Kirby TJ, Lammerding J (2018). Emerging views of the nucleus as a cellular mechanosensor. Nat Cell Biol 20, 373–381.
Koebel CM, Vermi W, Swann JB, Zerafa N, Rodig SJ, Old LJ, Smyth MJ, Schreiber RD (2007). Adaptive immunity maintains occult cancer in an equilibrium state. Nature 450, 903–907.
Lammerding J, Hsiao J, Schulze PC, Kozlov S, Stewart CL, Lee RT (2005). Abnormal nuclear shape and impaired mechanotransduction in emerin-deficient cells. J Cell Biol 170, 781–791.
Le HQ, Ghatak S, Yeung C-YC, Tellkamp F, Guenschmann C, Dieterich C, Yeroslaviz A, Habermann B, Pombo A, Niessen CM, Wickstroem SA (2016). Mechanical regulation of transcription controls Polycomb-mediated gene silencing during lineage commitment. Nat Cell Biol 18, 864–875.
Lehtimaki JI, Fenix AM, Kotila TM, Balistreri G, Paavolainen L, Varjosalo M, Burnette DT, Lappalainen P (2017). UNC-45a promotes myosin folding and stress fiber assembly. J Cell Biol 216, 4053–4072.
Li Z-H, Bresnick AR (2006). The S100A4 metastasis factor regulates cellular motility via a direct interaction with myosin-IIA. Cancer Res 66, 5173–5180.

Lombardi ML, Jaalouk DE, Shanahan CM, Burke B, Roux KJ, Lammerding J (2011). The interaction between nesprins and sun proteins at the nuclear envelope is critical for force transmission between the nucleus and cytoskeleton. J Biol Chem 286, 26743–26753.

Luxton GWG, Gomes ER, Folker ES, Vintinner E, Gundersen GG (2010). Linear arrays of nuclear envelope proteins harness retrograde actin flow for nuclear movement. Science 329, 956–959.

Malins DC, Anderson KM, Gilman NK, Green VM, Barker EA, Hellstroem KE (2004). Development of a cancer DNA phenotype prior to tumor formation. Proc Natl Acad Sci USA 101, 10721–10725.

Maninova M, Caslavsky J, Vomastek T (2017). The assembly and function of perinuclear actin cap in migrating cells. Protoplasma 254, 1207–1218.

Maninova M, Vomastek T (2016). Dorsal stress fibers, transverse actin arcs and perinuclear actin fibers form an interconnected network that induces nuclear movement in polarizing fibroblasts. FEBS J 283, 3676–3693.

Maniotis AJ, Chen CS, Ingber DE (1997). Demonstration of mechanical connections between integrins, cytoskeletal filaments, and nucleoplasm that stabilize nuclear structure (cell mechanics/cell engineering/tensegrity/extracellular matrix/mechanotransduction). Proc Natl Acad Sci USA 94, 849–854.

Mitra A, Mishra L, Li S (2013). Technologies for deriving primary tumor cells for use in personalized cancer therapy. Trends Biotechnol 31, 347–354.

Mizutani T, Haga H, Koyama Y, Takahashi M, Kawabata K (2006). Diphosphorylation of the myosin regulatory light chain enhances the tension acting on stress fibers in fibroblasts. J Cell Physiol 209, 726–731.

Newell-Litwa KA, Horwitz R, Lamers ML (2015). Non-muscle myosin II in disease: mechanisms and therapeutic opportunities. Dis Models Mech 8, 1495–1515.

Pecci A, Ma X, Savoia A, Adelstein RS (2018). MYH9: structure, functions and role of non-muscle myosin IIA in human disease. Gene 664, 152–167.

Qin Z, Kim H-J, Hemme J, Blankenstein T (2002). Inhibition of methylcholanthrene-induced carcinogenesis by an interferon γ receptor-dependent foreign body reaction. J Exp Med 195, 1479–1490.

Quail DF, Joyce JA (2013). Microenvironmental regulation of tumor progression and metastasis. Nat Med 19, 1423–1437.

Rajgor D, Shanahan CM (2013). Nesprins: from the nuclear envelope and beyond. Expert Rev Mol Med 15, 1–17.

Rosado LAR, Horn TA, McGrath SC, Cotter RJ, Yang JT (2011). Association between α4 integrin cytoplasmic tail and non-muscle myosin IIA regulates cell migration. J Cell Sci 124, 483–492.

Saha S, Dey SK, Das P, Jana SS (2011). Increased expression of nonmuscle myosin IIs is associated with 3MC-induced mouse tumor. FEBS J 278, 4025–4034.

Schramek D, Sendoel A, Segal JP, Beronja S, Heller E, Oristian D, Reva B, Fuchs E (2014). Direct in vivo RNAi screen unveils myosin IIa as a tumor suppressor of squamous cell carcinomas. Science 343, 309–313.

Shao X, Li Q, Mogilner A, Bershadsky AD, Shivashankar GV (2015). Mechanical stimulation induces formin-dependent assembly of a perinuclear actin rim. Proc Natl Acad Sci USA 112, E2595–E2601.

Shutova MS, Svitkina TM (2018). Mammalian nonmuscle myosin II comes in three flavors. Biochem Biophys Res Commun 506, 394–402.

Smith AS, Nowak RB, Zhou S, Giannetto M, Gokhin DS, Papoin J, Ghiran IC, Blanc L, Wan J, Fowler VM (2018). Myosin IIA interacts with the spectrin-actin membrane skeleton to control red blood cell membrane curvature and deformability. Proc Natl Acad Sci USA 115, E4377–E4385.

Tajik A, Zhang Y, Wei F, Sun J, Jia Q, Zhou W, Singh R, Khanna N, Belmont AS, Wang N (2016). Transcription upregulation via force-induced direct stretching of chromatin. Nat Mater 15, 1287–1296.

Takaoka M, Saito H, Takenaka K, Miki Y, Nakanishi A (2014). BRCA2 phosphorylated by PLK1 moves to the midbody to regulate cytokinesis mediated by nonmuscle myosin IIC. Cancer Res 74, 1518–1528.

Thakker DR, Levin W, Wood AW, Conney AH, Stoming TA, Jerina DM (1978). Metabolic formation of 1,9,10-trihydroxy-9,10-dihydro-3-methylcholanthrene: a potential proximate carcinogen from 3-methylcholanthrene. J Am Chem Soc 100, 645–647.

Thul PJ, Aakesson L, Wiking M, Mahdessian D, Geladaki A, Ait Blal H, Alm T, Asplund A, Bjoerk L, Breckels LM, *et al*. (2017). A subcellular map of the human proteome. Science 356, 820.

Totsukawa G, Yamakita Y, Yamashiro S, Hartshorne DJ, Sasaki Y, Matsumura F (2000). Distinct roles of ROCK (Rho-kinase) and MLCK in spatial regulation of MLC phosphorylation for assembly of stress fibers and focal adhesions in 3T3 fibroblasts. J Cell Biol 150, 797–806.

Vicente-Manzanares M, Horwitz AR (2010). Myosin light chain mono- and diphosphorylation differentially regulate adhesion and polarity in migrating cells. Biochem Biophys Res Commun 402, 537–542.

Vicente-Manzanares M, Ma X, Adelstein RS, Horwitz AR (2009). Non-muscle myosin II takes center stage in cell adhesion and migration. Nat Rev Mol Cell Biol 10, 778–790.

Wang S, Stoops E, Cp U, Reuveny A, Ordan E, Volk T, Markus B (2018). Mechanotransduction via the LINC complex regulates DNA replication in myonuclei. J Cell Biol 217, 2005–2018.

Wong SY, Ulrich TA, Deleyrolle LP, MacKay JL, Lin J-MG, Martuscello RT, Jundi MA, Reynolds BA, Kumar S (2015). Constitutive activation of myosin-dependent contractility sensitizes glioma tumor-initiating cells to mechanical inputs and reduces tissue invasion. Cancer Res 75, 1113–1122.

Zhang L, Li S, Gong Z, Jiang A, Ye M, Choi Y-L, Lee J, Liu X, Pei Y, Mao M, *et al*. (2017). Systematic identification of cancer-related long noncoding RNAs and aberrant alternative splicing of quintuple-negative lung adenocarcinoma through RNA-Seq. Lung Cancer 109, 21–27.

Zhang Q, Skepper JN, Yang F, Davies JD, Hegyi L, Roberts RG, Weissberg PL, Ellis JA, Shanahan CM (2001). Nesprins: a novel family of spectrin-repeat-containing proteins that localize to the nuclear membrane in multiple tissues. J Cell Sci 114, 4485–4498.

Zhen Y-Y, Libotte T, Munck M, Noegel AA, Korenbaum E (2002). NUANCE, a giant protein connecting the nucleus and actin cytoskeleton. J Cell Sci 115, 3207–3222.